scientific reports

Check for updates

OPEN

Synergistic Cu-Sb oxide electrocatalyst synthesized by sol-gel method for high-efficiency nitrate reduction to ammonia with suppressed hydrogen evolution

AliReza Babaei[1], Milad Rezaei[1]✉, Pirooz Marashi[1] & William Mark Rainforth[2]

Antimony is one of the hydrogen evolution poison and copper is one of the well-known catalysts for the nitrate reduction to ammonia (NRA). Therefore, to synthesize an efficient electrode that can have the highest selectivity for the reduction of nitrate to ammonia and is accompanied by the lowest hydrogen evolution, in this study, a combination of different Cu to Sb ratios was prepared on a Ti substrate using the sol-gel method in the form of crystalline oxides ($CuSb_yO_x$/Ti) to achieve the best catalytic activity and ammonia yield. A 2:1 ratio of Sb to Cu synthesized and calcined at 600 °C had the best catalytic properties. $CuSb_yO_x$/Ti electrocatalysts were evaluated for NRA in an alkaline medium. The $CuSb_2O_x$ electrocatalyst had the highest activity with the lowest cathodic Tafel constant of 78 mV dec^{-1}. EIS results also showed that $CuSb_2O_x$ has the lowest charge transfer resistance (R_{total}=3.75 Ω cm^2). The measurements revealed that the $CuSb_2O_x$ electrocatalyst performed superlative, with an NH_3 yield of 7280 μg h^{-1} cm^{-2} and an F.E. of 89% at a potential of -0.7 V vs. RHE. The high NH_3 yield of this oxide electrocatalyst, compared to other oxide compounds, highlights the synergistic effect of Cu and Sb.

Keywords Electrocatalyst, Electrocatalytic nitrate reduction to ammonia, NH_3 yield, Bimetallic, Ammonia synthesis

Ammonia is a widely used material for the production of a wide range of fertilizers, chemicals, and pharmaceuticals[1,2]. Due to its high energy density and hydrogen storage capacity, NH_3 can also be considered a renewable energy source[3]. Industrial production of NH_3 is of particular importance given the global demand for nitrogen-containing fertilizers for example ammonium nitrate (NH_4NO_3), urea ($CO(NH_2)_2$), and various nitrogen compounds. This sector has contributed significantly to increasing global food production by a factor of 7 to 8 since the beginning of the 20th century[4]. NH_3 is mainly generated by the well-known Haber-Bosch process[5]. However, the cleavage of the stable nitrogen-nitrogen bond (N ≡ N) in N_2, which is required for the reaction with hydrogen (H_2), takes place under harsh conditions of high temperature (between 400 and 600 °C) and pressure (~400 atm). This indicates the high energy consumption in the Haber-Bosch process[6]. Furthermore, ammonia production accounts for more than 1% of global energy consumption and contributes significantly to CO_2 emissions[7]. The hydrogen needed for ammonia synthesis is primarily obtained through coal gasification or natural gas reforming, processes that emit about 0.5 billion tons of CO_2 each year. Since Haber–Bosch process entails harsh conditions, intricate infrastructure, high energy intensity, and notable environmental impacts, it is crucial to address its shortcomings. In light of escalating energy demand and ongoing environmental challenges, it is imperative to develop environmentally friendly ammonia synthesis technology that operates under milder process[8]. The electrochemical nitrogen reduction reaction (NRR) offers several advantages, including lower energy consumption, a better carbon footprint, and a simpler reactor design[9,10], However, at high current densities, the electrochemical NRR process still exhibits a relatively low ammonia yield, significantly lower than that of the Haber-Bosch process. Therefore, replacing N_2 with nitrogen sources, especially nitrate/nitrite (NO_3^-/NO_2^-), is considered a promising option to reduce energy requirements, enhance ammonia production, and

[1]Department of Materials and Metallurgical Engineering, Amirkabir University of Technology (Tehran Polytechnic), Tehran 159163-4311, Iran. [2]Department of Materials Science and Engineering, University of Sheffield, Sir Robert Hadfield Building, Mappin Street, Sheffield, UK. ✉email: miladrezaei@aut.ac.ir

improve the energy efficiency of the system[11]. Nitrate/nitrite reduction to ammonia (NRA) offers an effective solution to address the energy crisis and control NO_3^-/NO_2^- contamination in wastewater. Due to the global use of nitrogen fertilizers, fossil fuel combustion, and wastewater discharge, large amounts of NO_3^- have been identified in surface and groundwater[12]. In order to protect health, the WHO and the U.S. EPA have set maximum permissible levels of 10 mg/L (NO_3^-) and 1 mg/L (NO_2^-) in drinking water[13]. Given the high NO_3^- content, the electrochemical eight-electron transfer in the nitrate reduction to ammonia is considered a more efficient process to address energy and environmental problems[14].

Various electrocatalytic systems have been developed for NRA, using heterogeneous catalysts based on different metals includes platinum group, copper, etc. However, at high potentials, the hydrogen evolution reaction (HER) dominates, which is unfavorable for the NRA process. In fact, the HER competes with the NRA, consuming electrons and reducing the overall efficiency. Therefore, the development of electrocatalysts that can selectively reduce NO_3^-/NO_2^- to NH_3 while simultaneously suppressing the HER is highly desirable[15–21]. However, the high cost and limited availability of noble metals have significantly hampered their development and widespread application. In contrast, base-metal-based electrocatalysts are more commonly used, making their development more desirable[22–24]. Furthermore, the development of new technologies for green ammonia synthesis (electrochemical reaction of nitrate/nitrite reduction to ammonia) is of great importance for human society[25–28].

The strong synergy between two components, optimizes the electron transport properties, tunes the active sites, and improves the efficiency of nitrate ion adsorption in the multicomponent oxide electrocatalyst. Recent studies have investigated multicomponent oxide electrocatalysis systems for the electrochemical synthesis of ammonia from nitrate, focusing on advanced catalysts to improve efficiency and stability[29,30]. Li and colleagues[30] investigated the formation of a two-dimensional heterogeneous compounds of copper and iron oxide, which enhanced the electrochemical performance by increasing the catalytic activity and improving the stability of nitrate reduction. Tang and colleagues[31] developed a heterogeneous CoO-CuO_x structure for the electrochemical nitrate reduction to ammonia. This heterogeneous structure combined the properties of cobalt oxide (CoO) and copper oxide (CuO_x), thus improving the electrochemical efficiency. The heterostructure of CoO-CuO_x demonstrated high efficiency in nitrate reduction and benefited from increased surface area and improved electrical conductivity, while exhibiting good stability under various reaction conditions. Furthermore, Huang et al.[32] introduced 3D flower-like zinc cobaltite ($ZnCo_2O_4$) as an impressive electrocatalyst for the NRA. This structure offered a high surface area, enabled facile electron/ion transfer, and significantly improving the electrochemical performance. The system demonstrated high efficiency and stability under ambient conditions, making it a promising catalyst for environmental and industrial applications. Further advances in electrocatalysis were reported by Hai et al.[33]. They introduced $NiCoO_2$ nanoarrays on copper foam, which demonstrated effective catalysis for the nitrate reduction to ammonia (NRA). The copper foam acted as a three-dimensional support increasing the active surface area and stability of the catalyst over time, thus significantly improving the electrochemical performance.

It should be noted that the performance of NRA systems can be significantly improved, but their practical application still presents several challenges. Due to the competitive reaction of HER during NRA, the selectivity and Faradaic efficiency of electrocatalysts remain important challenges. In this study, we will incorporate copper, a widely used element in NRA processes, along with antimony as a hydrogen release inhibitor (since this element can prevent the hydrogen (H_2) evolution[34], into the electrocatalyst composition. Copper acts as the active element for NRA, while antimony suppresses hydrogen gas production and provides stability in the system. This study demonstrates that the synergy between copper oxide and antimony oxide (copper antimonates) creates a powerful catalyst for the nitrate reduction to ammonia. The electrocatalytic stability, NO_3^- conversion, and selectivity for different molar ratios of antimony to copper, from Sb: Cu = 0.5 to 2.5, in the NRA process were evaluated. Copper antimonate ($CuSb_2O_X$ with Sb: Cu = 2) in 0.1 M NaOH with 0.1 M $NaNO_3$ achieves a Faradaic efficiency of 89% and an NH_3 yield of 7320 μg hr^{-1} cm^{-2} at optimum working potential of −0.7 V vs. RHE.

Results and discussion

Morphology, chemical composition, and structure of the electrocatalysts

FESEM, elemental mapping, and EDS results for $CuSb_{2.5}O_x$, $CuSb_2O_x$, $CuSb_{1.5}O_x$, $CoSbO_x$, and $CuSb_{0.5}O_x$ are shown in Fig. 1. FESEM images showed that the morphology of each electrocatalyst, depending on the ratio of Sb to Cu, differed from the others. The FESEM images at higher magnification (Fig. S3) show that the particles that make up the electrode contain a 2:1 ratio of Sb to Cu ($CuSb_2O_x$ electrocatalyst), is in the range of 50 to 120 nm. Figure 1 and the EDS-Mapping results also demonstrate that the elements are evenly distributed throughout the coating. Fig. S4 shows the FESEM image along with the EDS-mapping of the cross-section of the coating. As can be seen in Fig. S4, the coating thickness from the set of measurements (according to ASTM B487) was 38.0 ± 4.4 μm, indicating an acceptable uniformity of the coating on the electrode surface. To obtain a more precise chemical composition of the electrocatalysts, ICP-MS was used in addition to EDS analysis. Table 1 shows the EDS and ICP results for each electrocatalyst. According to the EDS and ICP results, the copper and antimony concentrations in the coating are consistent with the precursors during the synthesis of $CuSb_2O_x$ and $CuSb_{1.5}O_x$. However, the stoichiometric ratio of antimony to copper in other compounds is not necessarily the same as its amount in the precursor solution, which may be due to the difference in the evaporation rate of chloride salts at different molar ratios of Sb to Cu. In addition, it should be noted that the amount of oxygen in these compounds, due to the weakness of EDS in detecting elements lighter than sodium, cannot be the same as its actual amount, and therefore, X-ray diffraction must be employed to detect the chemical composition of the formed mixed oxide. PXRD patterns of catalysts synthesized from different molar ratios of antimony and copper are shown in Fig. 2. According to Fig. 2, $CuSb_2O_6$ is the main phase. Figure 2 shows that, as expected, the compound with a molar ratio of 2:1 antimony to copper exhibits the highest percentage of the $CuSb_2O_6$ phase.

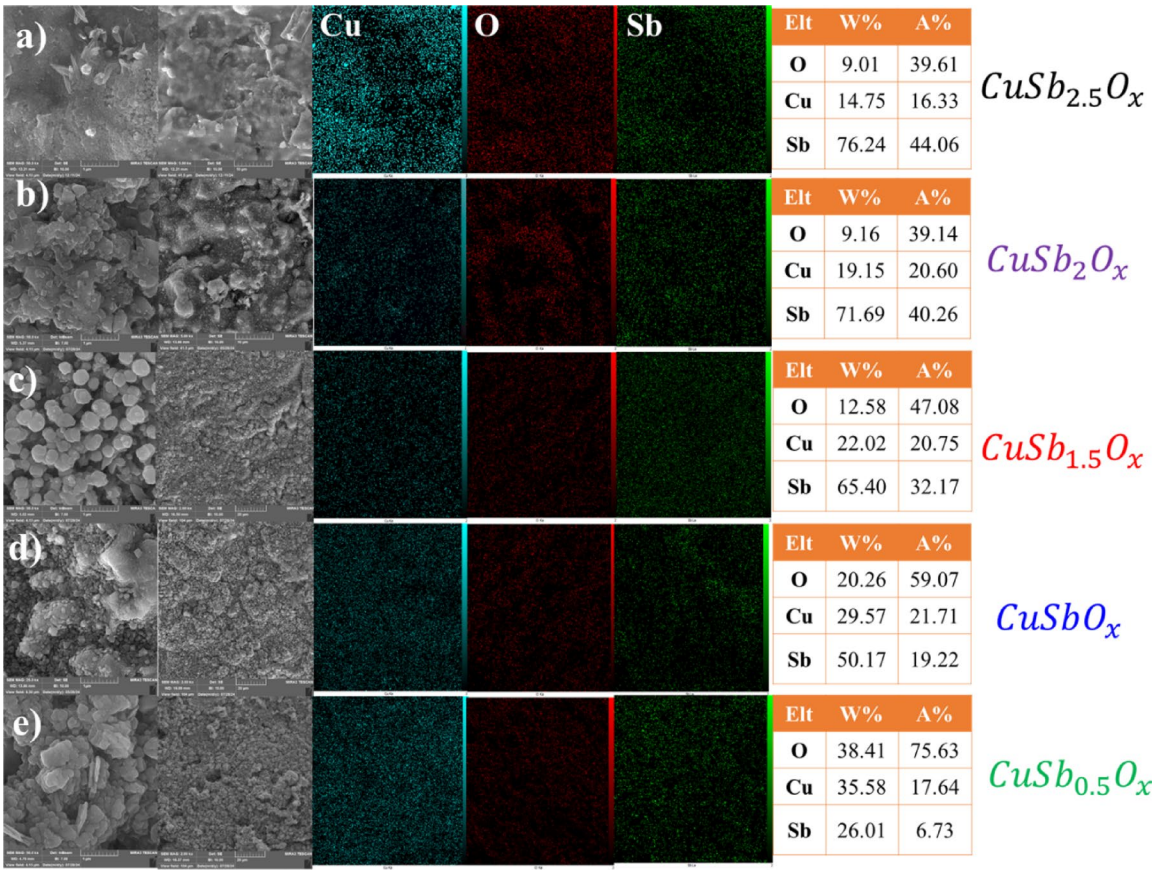

Fig. 1. SEM images, elemental mapping, and EDS analysis results (atomic percentage and weight%) for **a**) $CuSb_{2.5}O_x$, **b**) $CuSb_2O_x$, **c**) $CuSb_{1.5}O_x$, **d**) $CoSbO_x$ and **e**) $CuSb_{0.5}O_x$.

Electrocatalyst	ICP			EDS		
	Cu (ppm)	Sb (ppm)	Sb: Cu (at./at.)	Cu (at%)	Sb (at%)	Sb: Cu (at./at.)
$CuSb_2O_x$	388.91	1510.4	**2.03**	20.60	40.26	**1.95**
$CuSb_{1.5}O_x$	440.03	1199.3	**1.42**	20.75	32.17	**1.55**
$CuSbO_x$	503.21	892.22	**0.93**	21.71	19.22	**0.89**
$CuSb_{0.5}O_x$	712.37	409.69	**0.30**	17.64	6.73	**0.38**
$CuSb_{2.5}O_x$	284.32	1608.1	**2.95**	16.33	44.06	**2.70**

Table 1. Comparison of EDS and ICP results for determining the molar ratio of copper and antimony in the chemical composition of electrocatalysts.

At a ratio of 2.5:1, the excess antimony appears as the oxide phases of Sb_2O_4 and/or Sb_2O_5. At ratios of 1:1 and 1.5:1, the excess copper is observed as divalent copper oxide. However, at a ratio of 0.5:1, the target phase is not visible, and the $Cu_9Sb_4O_{19}$ phase is displayed along with CuO as the main phases. It is very likely that the lack of formation of $CuSb_2O_6$ phase could be the reason for the lack of suitable electrocatalytic performance for this compound (see Sect. 3.2.).

On the other hand, the PXRD pattern of $CuSb_2O_6$ revealed a slightly distorted monoclinic phase (space group $P2_1/n$) with lattice constants a = b = 4.643 Å, and c = 9.299 Å. In the tri-rutile structure of $CuSb_2O_6$, the triplication of the c axis generates in a lattice of CuO_6 and SbO_6 octahedra split at the edges and corners. Arrays of magnetic Cu^{2+} are sandwiched between layers of diamagnetic Sb^{5+}, which creates quasi-one-dimensional antiferromagnetism through an in-plane super-exchange mechanism. According to the Jahn–Teller distortion of Cu^{2+}[35], $CuSb_2O_6$ occurs in two polymorphs, α and β, which are distinguished primarily by the way in which the CuO_6 octahedra are compressed or stretched. The β polymorph is characterized by a distortion perpendicular to the one-dimensional magnetic chain, while α-$CuSb_2O_6$ exhibits octahedral compression along the chain. The aforementioned changes cause the $CuSb_2O_6$ compound to crystallize in both the α- and β-states, namely tetragonal ($P4_2/mnm$) and monoclinic ($P2_1/n$), respectively[35–38]. In this study, after calcination of all the

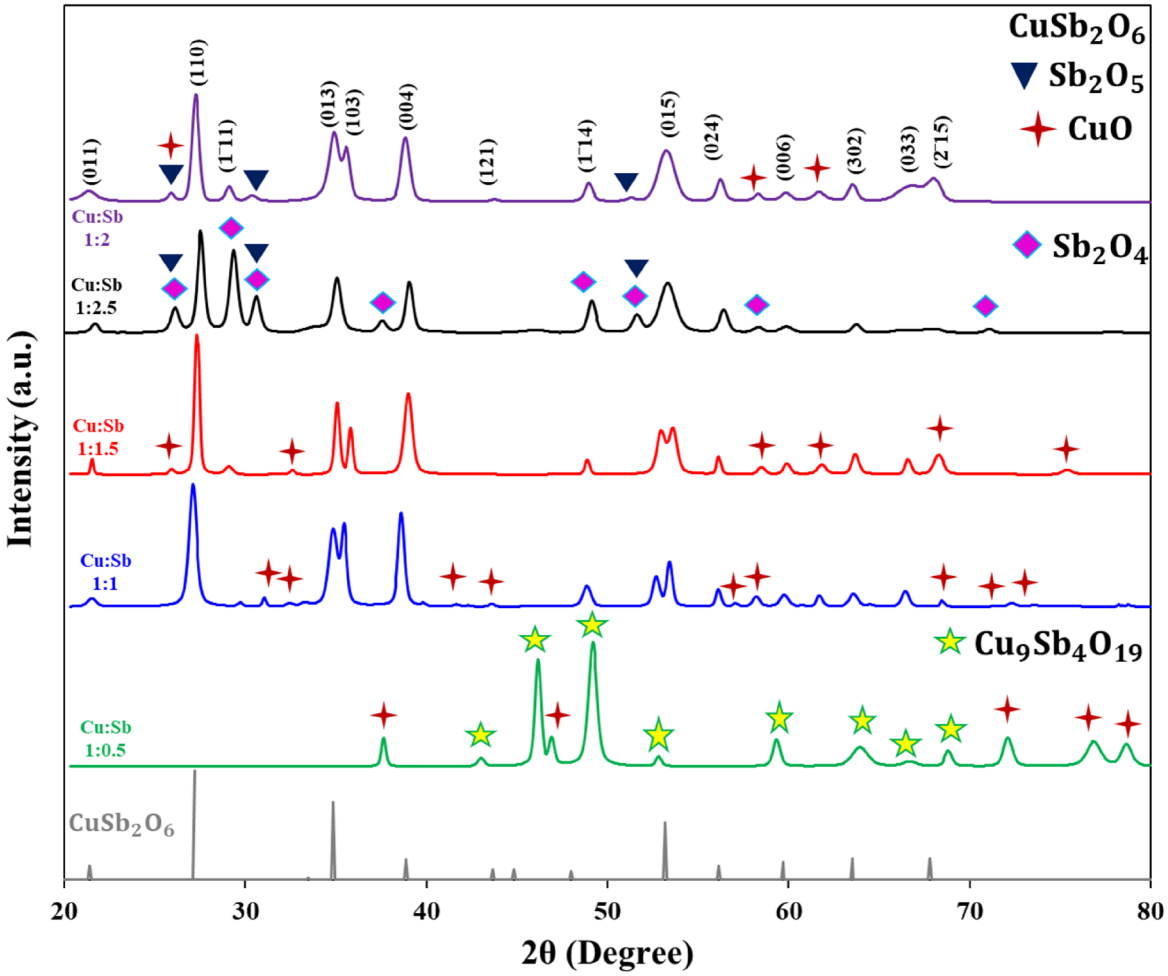

Fig. 2. PXRD patterns for the $CuSb_2O_x$ (purple), $CuSb_{2.5}O_x$ (black), $CuSb_{1.5}O_x$ (red), $CuSbO_x$ (blue), and $CuSb_{0.5}O_x$ (green) compounds calcined at 600 °C along with phase identification.

electrocatalysts at 600 °C, $CuSb_2O_6$ transformed from the α-polymorphic tri-rutile structure ($P4_2/mnm$) to the β form, which crystallizes in the monoclinic space group $P2_1/n$.

Electrocatalytic activity, cathodic Tafel Constant (β_c), electrochemical active surface area, and charge transfer resistance of $CuSb_yO_x$

The LSV curves in Fig. 3a show that the presence of nitrate ions in the solution causes a significant increase in the cathodic current density values, indicating a strong reduction reaction at the surface of the electrocatalysts. For the $CuSb_{0.5}O_x$ electrocatalyst, the current increase at more positive potentials is due to the partial reduction of copper oxide due to the presence of excess copper oxide based on PXRD results. For all electrocatalysts, the nitrate reduction current density is observed at a potential of approximately − 0.5 V vs. RHE[39]. It is noteworthy that the LSV curves of the $CuSb_2O_x$ electrocatalyst, in presence and absence of nitrate ions, shows the largest change compared to the other electrocatalysts. Moreover, increasing the antimony to copper ratio to 2:1 shows the best electrocatalyst activity in term of reaction rate. The LSV results of CuO_x and SbO_x along with the optimal ratio of copper and antimony ($CuSb_2O_x$) are presented in Fig. S5. As can be seen in Fig. S5, CuO_x shows a broad peak indicating the reduction of Cu^{2+} to Cu^+ and Cu^0. In contrast, SbO_x does not exhibit suitable electrocatalytic activity and due to the lack of reduction of antimony oxide in an aqueous environment, its composition remains constant. The combination of a 2:1 ratio of antimony to copper in $CuSb_2O_x$ resulted in a significant increase in electrocatalytic activity, and almost no trace of the copper ion reduction peak is observed in the $CuSb_2O_x$ electrocatalyst, which confirms the synergistic role of the simultaneous presence of Cu and Sb. The activity of the $CuSb_2O_x$ and $CuSb_{1.5}O_x$ electrocatalysts was measured at different nitrate concentrations, 0.010 M to 0.100 M NO_3^-, which shows the good activity[33] of the $CuSb_2O_x$ electrocatalyst for the NRA process as shown in Fig. S6 a. This study (Fig. 6a and b) confirms the assignment of the cathodic peak of nitrate reduction at a potential of −0.5 vs. RHE for the $CuSb_yO_x$ electrocatalysts at different nitrate concentrations.

Figure 3b shows the Tafel diagrams obtained from the LSV curves. According to the Tafel diagrams, the $CuSb_2O_x$ electrocatalyst exhibits the best catalytic activity, differing significantly (at least 3 times) from the other

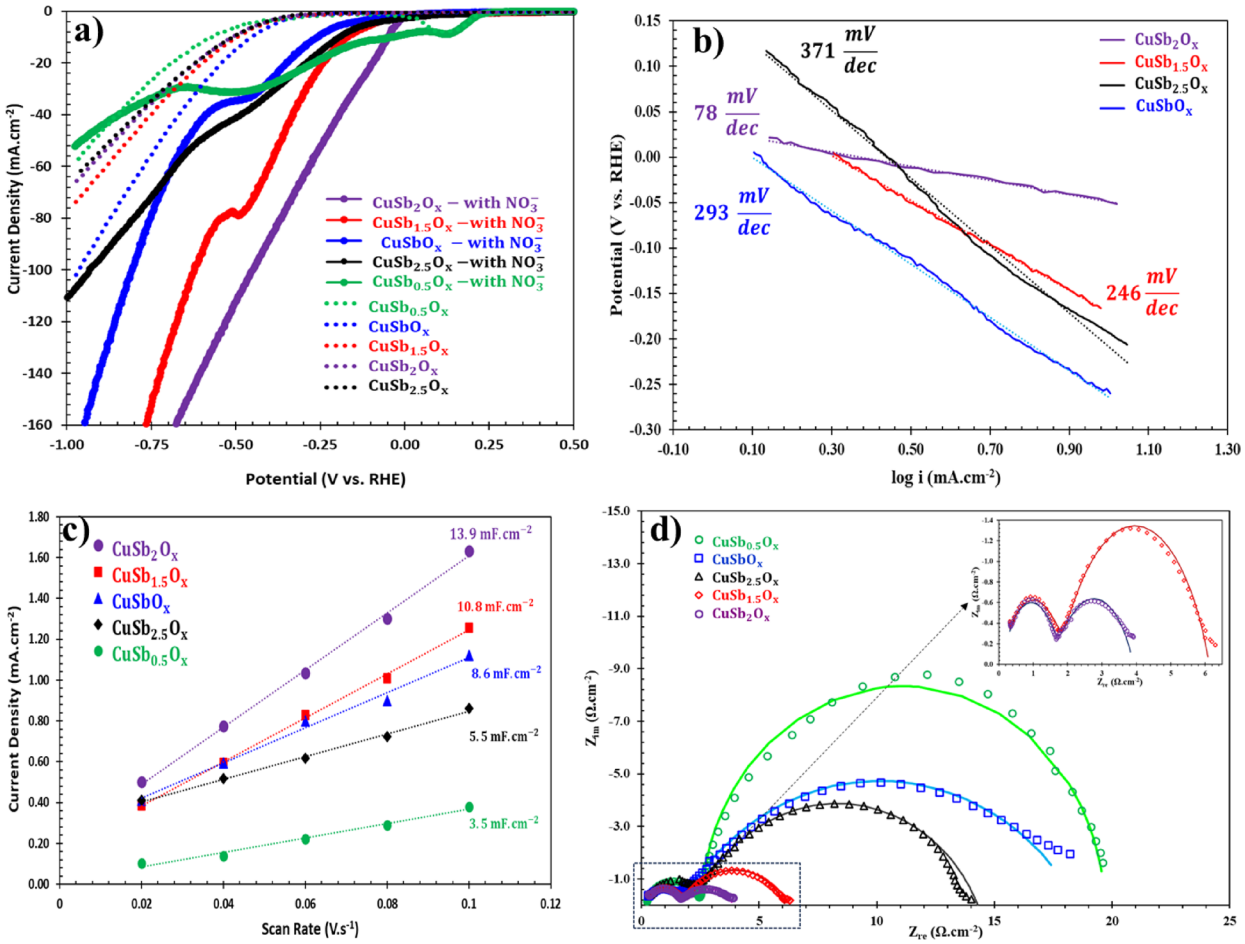

Fig. 3. **a**) LSV curves in 0.1 M NaOH with and without 0.1 M $NaNO_3$. **b**) Tafel diagrams. **c**) ECSA curves (double layer capacitance values) and **d**) Nyquist diagrams of the EIS results along with the data fitting for the various synthesized electrocatalysts.

electrocatalysts. Based on the copper oxide reduction peak in the LSV diagram of the $CuSb_{0.5}O_x$ electrocatalyst, it was not possible to calculate the cathodic Tafel constant for it.

The ECSA of the copper antimonate electrocatalysts were estimated based on the electric double layer capacitance (C_{dl}) (Fig. 3c). Figure 3c shows that $CuSb_2O_x$ has the largest specific capacitance. This demonstrates the higher the ECSA, and as result the better the electrochemical NRA process. It is likely the large ECSA is not simply due to the high specific surface area, but rather due to the appropriate arrangement of Sb and Cu within the oxide structure, the active sites on the surface for the adsorption of electroactive ions have increased; especially since, as we know, the atomic sites of transition metals within the antimonate phase can be suitable sites for the ad-desorption of electroactive species[40]. The corresponding small amplitude cyclic voltammograms in the non-Faradaic domain at various scan rates are shown in Fig. S7.

The Nyquist diagrams of the electrochemical impedance spectroscopy are shown in Fig. 3d. The equivalent circuit obtained by fitting the experimental data, which includes two time-constants, is shown in Fig. S8. The parameters obtained from the EIS data fitting are listed in Table 2. Considering the complex mechanism and multiple half-reactions of the NRA process, it is likely that the charge transfer resistance 1 (R_{ct1}) appearing in the Nyquist diagrams is related to reaction (1) and the charge transfer resistance 2 (R_{ct2}) for reaction (6). These two half-reactions are likely to be the slowest half-reactions of the NRA process[41,42]. Nitrate has a high-energy antibonding orbital, and electron transfer from the electrode to this orbital requires crossing a significant energy barrier. This leads to a very small exchange current from a kinetic perspective which results in, a high charge transfer resistance. Experimental evidence, including a Tafel slope of about 120 mV dec^{-1}, indicates that this single-electron step acts as the rate-determining step in the nitrate → nitrite branch[41]. In the reduction of nitrogenous intermediates to ammonia, the first steps of NO reduction are also the most critical and slowest[42]. The first step is the protonation/reduction of NO and is electronically challenging, because NO is a relatively stable radical with a half-filled orbital and its conversion to HNO requires electronic rearrangement and a change in the N–O bonding state. Hence, reaction (6) represents the bottleneck of the NO → NOH_3 (ads) branch[41]. Due to the nature of these two slow steps, their effect also appears as two distinct loops in the Nyquist plot in EIS. Each of the rate-limiting steps, which involve slow charge transfer, introduces a distinct time constant and a significant charge transfer resistance. Therefore, the first time-constant is usually attributed to reaction (1),

Electrocatalyst	R_s (Ω.cm²)	R_{ct1} (Ω.cm²)	Y_{CPE} ($\Omega^{-1}.cm^{-2}.s^n$)	n	R_{ct2} (Ω.cm²)	Y_{CPE} ($\Omega^{-1}.cm^{-2}.s^n$)	n	R_{total} (Ω.cm²)
$CoSb_{2.5}O_x$	0.1	2.3	2×10^{-4}	0.75	11.9	5×10^{-3}	0.73	14.2
$CoSb_2O_x$	0.14	1.5	9.1×10^{-5}	0.82	2.25	3×10^{-2}	0.65	3.75
$CoSb_{1.5}O_x$	0.1	1.7	1.1×10^{-4}	0.78	4.3	1.6×10^{-2}	0.71	6.0
$CoSbO_x$	0.1	1.6	2.1×10^{-4}	0.75	16.9	1×10^{-2}	0.65	18.5
$CoSb_{0.5}O_x$	0.1	2.4	9×10^{-5}	0.84	17.1	7×10^{-3}	0.98	19.5

Table 2. Parameters determined from the EIS data for the synthesized electrocatalysts at a potential of −0.4 V vs. RHE.

which is the slowest step of the nitrate → nitrite branch, and the second time-constant is attributed to reaction (6) (or the sum of the initial steps NO → NOH_3 (ads)). Since these two steps have the highest energy barrier and the smallest exchange current, the charge transfer resistance associated with them is separable in the impedance spectrum and is observed as two distinct loops.

The $CuSb_2O_x$ electrocatalyst has the lowest total resistance (R_{total}) of 3.75 Ω cm², indicating good electrocatalytic activity for the NRA process. This is in perfect agreement with the LSV results and the Tafel diagrams.

$$NO_3^- (ads) + e \rightarrow NO_3^{2-} (ads) \qquad E^0 = -890\ mV \text{ versus SHE} \tag{1}$$

$$NO_3^{2-} (ads) + H_2O \rightarrow NO_2 (ads) + 2OH^- \tag{2}$$

$$NO_2 (ads) + e \rightarrow NO_2^- (ads) \qquad E^0 = 1040\ mV \text{ versus SHE} \tag{3}$$

$$NO_2^- (ads) + e \rightarrow NO_2^{2-} (ads) \qquad E^0 = -470\ mV \text{ versus SHE} \tag{4}$$

$$NO_2^{2-} (ads) + H_2O \rightarrow NO (ads) + 2OH^- \tag{5}$$

$$NO (ads) + H^+ + e \rightarrow NOH (ads) \qquad E^0 = -780\ mV \text{ versus SHE} \tag{6}$$

$$NOH (ads) + H^+ + e \rightarrow NOH_2 (ads) \qquad E^0 = 520\ mV \text{ versus SHE} \tag{7}$$

$$NOH_2 (ads) + H^+ + e \rightarrow NOH_3 (ads) \qquad E^0 = 900\ mV \text{ versus SHE} \tag{8}$$

Considering that the electrocatalyst is applied as a coating on the titanium sheet and due to the porosity, the solution can access limited areas of the substrate, in accordance with the electrochemical investigations, several points indicate that the LSV and EIS signals are mainly due to the $CuSb_yO_x$ coating and the contribution of the titanium substrate to the electrochemical response is negligible. First, titanium in the medium used (nitrate-containing solution) exhibits minimal electrochemical activity in the cathodic potential region, especially at potentials below − 1 V vs. RHE (Fig. S5), and in this potential range, cathodic reactions primarily occur on the Cu–Sb oxide phase. This is fully consistent with the LSV results, since all changes and enhancements in the current (including the completely distinct behavior of $CuSb_2O_x$ compared to the other two compounds) are directly related to the presence and structure of the coating.

Second, the EIS data also show that the charge transfer resistance and extracted time constants are related to the NRA half-reactions (Rct1 and Rct2). The two Nyquist loops obtained are in perfect agreement with the multi-step mechanism of the NRA process, and in case of significant titanium contribution, a different spectral pattern (such as a dominant series resistance or a quasi-capacitive response of the TiO_2 structure) would have been expected. However, based on Fig. 3 d and the equivalent circuit in Fig. S8, both time constants are consistent with the electrocatalytic reactions of $CuSb_yO_x$ and the very low total resistivity of $CuSb_2O_x$ (3.75 Ω cm²) indicates the dominance of the active coating on the electrode behavior.

Third, the pattern of ECSA changes (Fig. 3c) and double layer capacitance is completely consistent with the change in Sb/Cu ratio, and if the substrate had a significant role in the electrochemical response, such a composition-structure-activity dependence would not be systematically observed. These results indicate that the effective surface area and active sites in the $CuSb_2O_x$ coating, not the substrate, are the main factors in the electrochemical response.

Performance of $CuSb_yO_x$ in nitrate reduction to ammonia (NRA)

The performance of copper antimonate electrocatalysts in NRA was investigated using chronoamperometry (CA) at a constant potential of −0.4 V vs. RHE (the potential before the sudden current increase in LSV diagrams without nitrate) (Fig. 4a). Experimental data show that the NH_3 yield (6280 μg h^{-1} cm^{-2}) and F.E. (87%) of the $CuSb_2O_x$ electrocatalyst are significantly higher than those of $CuSb_{1.5}O_x$ (NH_3 yield = 5860 μg h^{-1} cm^{-2}, FE = 81%), $CuSb_{2.5}O_x$ (NH_3 yield = 5190 μg h^{-1} cm^{-2}, FE = 71%), $CuSbO_x$ (NH_3 yield = 4905 μg h^{-1} cm^{-2}, FE = 67%) and $CuSb_{0.5}O_x$ (NH_3 yield = 1450 μg h^{-1} cm^{-2}, FE = 33%).

Figure 4b shows the electrochemical nitrate reduction to ammonia for the $CuSb_2O_x$ electrocatalyst at different applied potentials, thus highlighting the positive performance of $CuSb_2O_x$ in nitrate conversion. Figure 4b shows

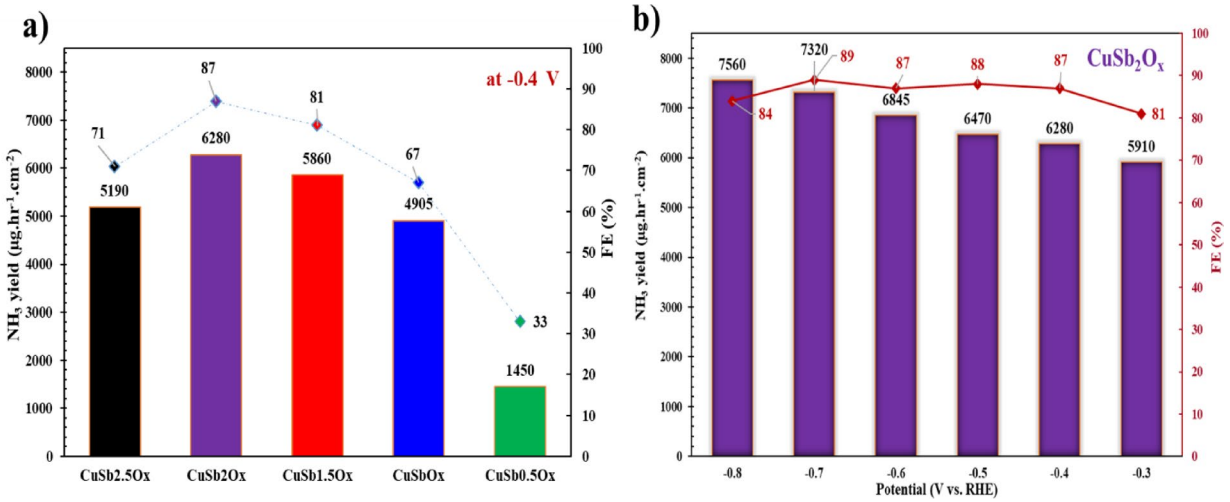

Fig. 4. **a**) NH_3 yield and Fes of $CuSb_yO_x$ at −0.4 V vs. RHE. **b**) NH_3 yield and Fes of $CuSb_2O_x$ at different given potentials.

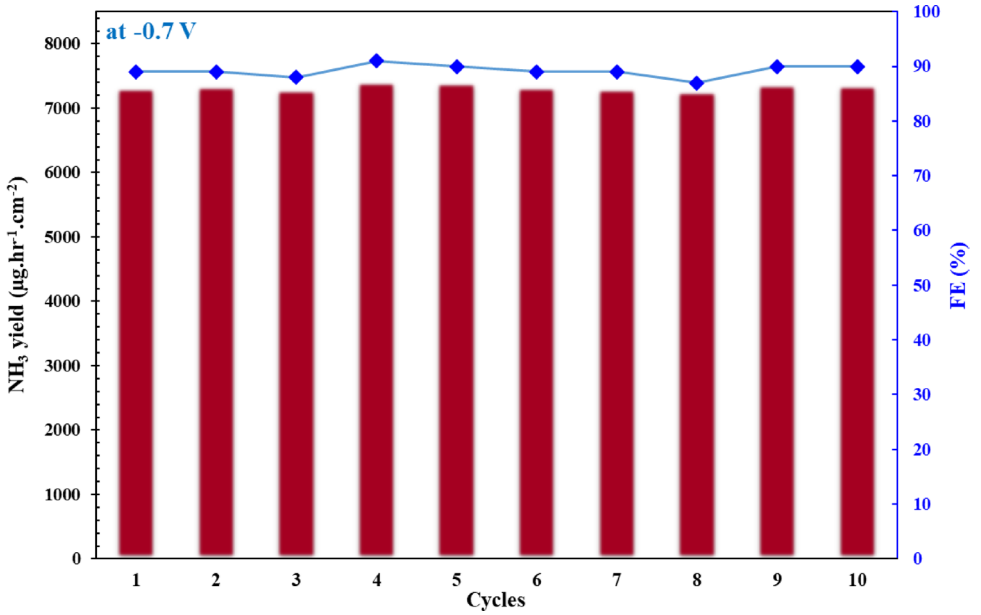

Fig. 5. Durability of $CuSb_2O_x$ electrocatalyst during 10 cycles at −0.7 potential vs. RHE.

that the increase in potential correlates well with the increase in nitrate reduction (conversion). At a potential of −0.7 V vs. RHE the ammonia yield increases to 7320 μg h^{-1} cm^{-2} and the FE increases to 89%. The reason for the FE reduction at a potential of −0.8 V vs. RHE is the relative dominance of the HER over NRA as seen in the LSV curves (Fig. 3a).

In addition to the catalytic performance of $CuSb_2O_x$, its electrocatalytic stability was also investigated (Fig. 5). Continuous cycling experiments were conducted at a potential of −0.7 V vs. RHE (the optimum potential from Fig. 4b). During 10 NRA cycles, the ammonia and FE yields for the electrocatalyst fluctuated within a narrow range, indicating that $CuSb_2O_x$ possesses favorable electrocatalytic stability. In addition, the changes in the concentrations of NO_3^- and NH_3 in the electrolyte over time were investigated (Fig. 6a). At a potential of −0.7 V vs. RHE, after 15 h of reaction, the concentrations of nitrate and ammonia in the solution were 26 mM and 73.5 mM, respectively. These results demonstrate that after 15 h of continuous catalytic reaction in 70 mL of electrolyte, a significant fraction of $NO_3^- - N$ is efficiently converted to NH_3-N. This study also demonstrates the electrocatalytic stability of $CuSb_2O_x$. Figure 6b shows the calculation results of the NO_3^- conversion rate and NH_3 selectivity during the 15-hour NRA process. The results demonstrate a continuous increase in the NO_3^- conversion rate during NRA and a continuous increase in NH_3 selectivity. The reason for the increase in selectivity over time is likely related to the removal of unstable oxides on the electrode surface and the presence

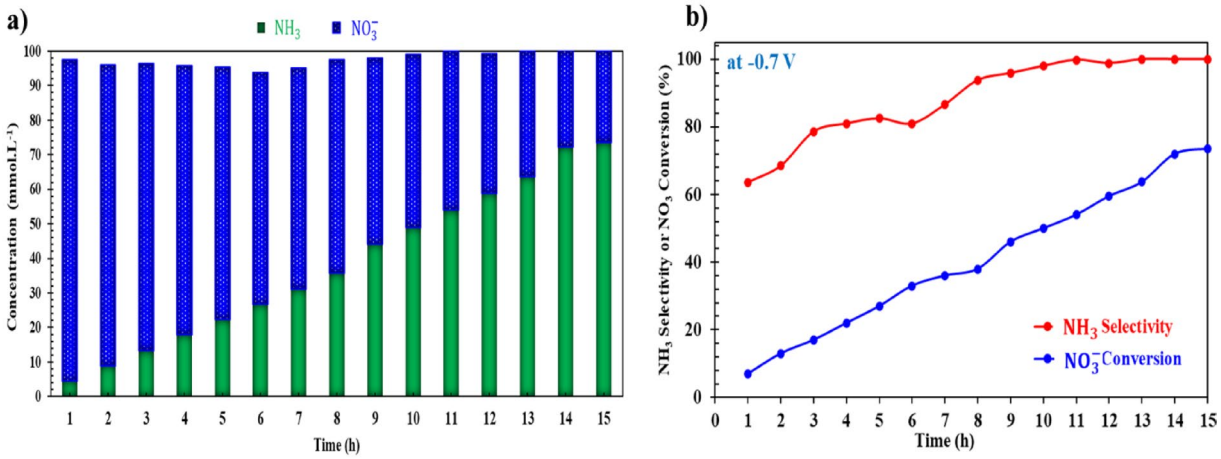

Fig. 6. **a**) Concentrations of $NO_3 - N$ and NH_3-N after the 15 h NRA process. **b**) Conversion of NO_3^- and selectivity of NH_3 during the 15 h NRA process.

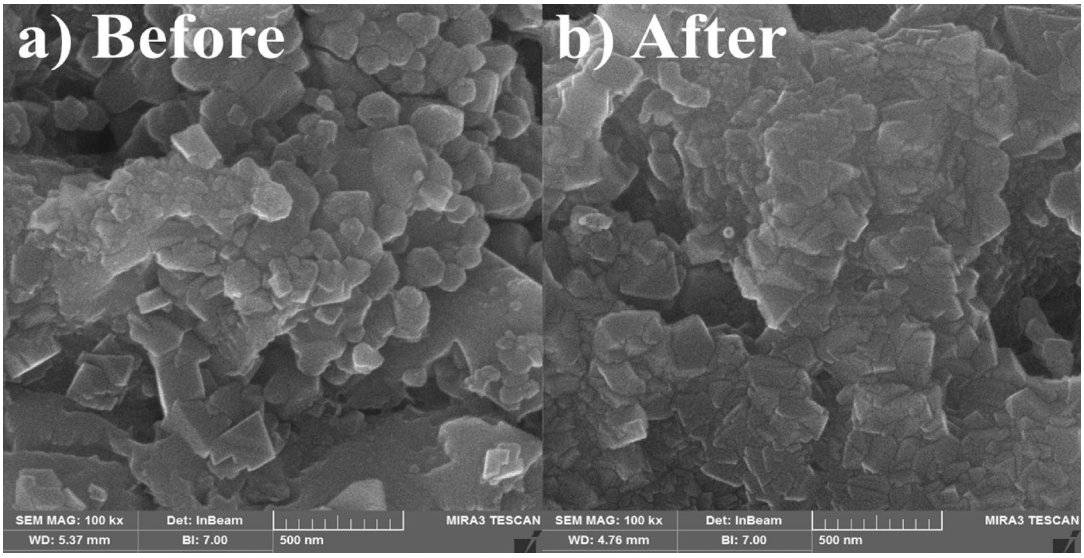

Fig. 7. FESEM images for the $CuSb_2O_x$ electrocatalyst **a**) before and **b**) after 15 h of NRA process.

of $CuSb_2O_6$ as the main single-phase facilitator of the nitrate reduction reaction. After 15 h of NRA, the NH_3 selectivity reached 98.8%, confirming the highly efficient and continuous conversion of NO_3^- to NH3 on the surface of the $CuSb_2O_x$ electrocatalyst. According to the FESEM images (Fig. 7), the original morphology of the electrocatalyst is approximately preserved after 15 h of NRA. The morphology of $CuSb_2O_x$ remains intact, further demonstrating its stability. This is consistent with the XRD results before and after NRA (Fig. 8). According to Fig. 8, the main phase $CuSb_2O_6$ remained stable after chronoamperometry, however, the CuO phase was not observed in the electrocatalyst composition. This was due to the dissolution of copper oxide, for example as form of $Cu(OH)_3^-$ ions and water molecules, during chronoamperometry.

According to Figs. 7 and 8 results, the gradual increase in NH_3 selectivity in Fig. 6b can be attributed to the gradual elimination of unstable CuO_x phases and the remaining stable and active $CuSb_2O_6$ phase. This phase plays a major role in the nitrate reduction reaction and its dominant presence over time leads to a continuous increase in NH_3 selectivity. The preservation of the surface morphology and structural stability in FESEM images and the preservation of the $CuSb_2O_6$ phase in XRD supports this interpretation. Therefore, the results show that the correlation between the improvement of selectivity performance and the structural stability of the catalyst during the reaction was due to the stabilization of the active $CuSb_2O_6$ phase and the removal of unstable surface species (such as CuO).

Table 3 compares the ammonia yield and Faradaic efficiency for nitrate reduction with some recent multicomponent electrocatalysts. It can be seen that the Faradaic efficiency for $CuSb_2O_x$ electrocatalysts is higher than that of other electrocatalysts. The ammonia yield of $CuSb_2O_x$ electrocatalysts is much higher

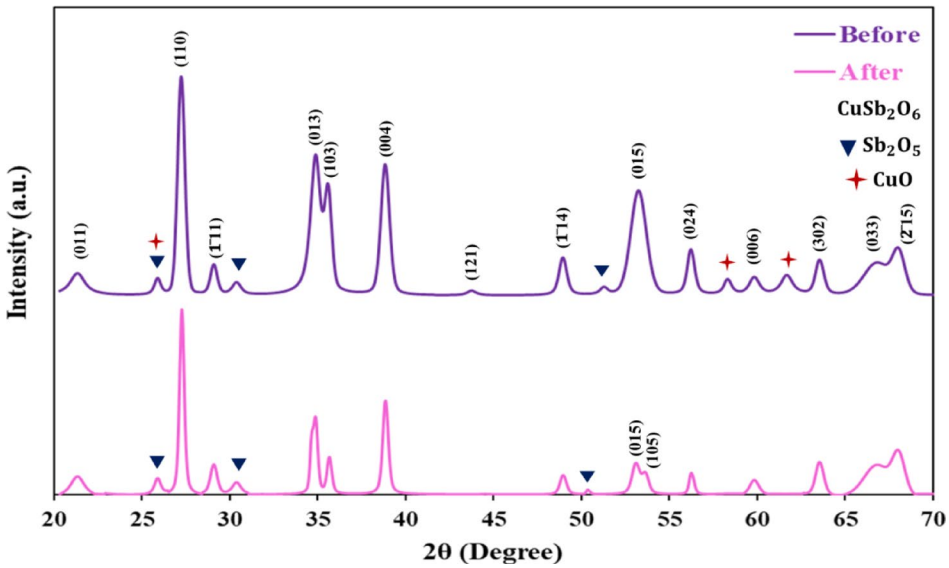

Fig. 8. XRD patterns for the $CuSb_2O_x$ electrocatalyst before and after 15 h of NRA process.

electrocatalyst	Potential (V vs. RHE)	NH_3 yield	FE (%)	Electrolyte	Ref.
Co-Fe@Fe_2O_3	−0.745	880.5 μg h^{-1} cm^{-2}	85	0.1 M Na_2SO_4 + 500 ppm NO_3^-	45
$Cu_{0.65}Pd_{0.35}O_x$	−0.2	1141 μg h^{-1} cm^{-2}	74	0.1 M KNO_2 + 0.1 M KNO_3	46
$ZnCo_2O_4$	−0.6	2100 μg h^{-1} cm^{-2}	80	0.1 M KOH + 0.1 KNO_3	32
$La_xFeO_{3-\delta}$	−0.8	1025 μg h^{-1} cm^{-2}	78	0.1 M Na_2SO_4 + 0.1 M $NaNO_3$	45
Cu-PTCDA	0.4	521 μg h^{-1} cm^{-2}	86	0.1 M PBS + 500 ppm NO_3^-	46
10Cu/TiO_{2-x}	−0.75	1943 μg h^{-1} mg_{cat}^{-1}	81	0.5 M Na_2SO_4 + 200 ppm NO_3^-	47
$B_{2.6}C$@TiO_2	−0.9	3679 μg h^{-1} cm^{-2}	88	0.1 M Na_2SO_4 + 0.5 mM Fe^{2+}-EDTA	48
Pd/Co_3O_4	−0.645	3400 μg h^{-1} cm^{-2}	89	0.5 M K_2SO_4 + 200 ppm NO_3^-	49
Bi_2S_3/MoS_2	−0.8	2550 μg h^{-1} cm^{-2}	88	0.1 M Na_2SO_4 + 0.1 M $NaNO_3$	50
$CuSb_2O_x$	−0.7	7320 μg h^{-1} cm^{-2}	89	0.1 M NaOH + 0.1 M $NaNO_3$	This work

Table 3. Comparison of ammonia yield and Faradaic efficiency in nitrate reduction by some newer multicomponent electrocatalysts.

(several times higher) than that of other electrocatalysts, even though it is synthesized on a plate substrate, as well. This comparison shows that the $CuSb_2O_x$ multicomponent electrocatalyst has well enhanced the ammonia production rate with the synergy of copper and antimony.

Experimental

Synthesis of electrocatalysts

Due to good dimensional stability, a grade 2 titanium (Ti-G2) plate was chosen as the substrate. The titanium plate was first sandblasted and then placed in a 10 wt% oxalic acid solution at 100℃ for complete etching. This was intended to create a rough surface and improve coating adhesion[51]. The starting solution was prepared using the Pechini method[52]. Ethylene glycol and citric acid were used as solvents. Once the solution reached 60℃, copper chloride and antimony chloride salts were added to the solution. Five solutions were prepared with antimony to copper molar ratios of 0.5, 1, 1.5, 2 and 2.5. The solutions were stirred for 1 h until completely homogenous. The solutions were applied to etched titanium with a brush and then placed in a 200 °C oven to completely evaporate the ethylene glycol solution. To induce the crystallization of copper antimony, a furnace heat treatment (600 °C, 7 min) was applied to the electrodes. Brushing was repeated 10 to 15 times to completely cover the electrode surface with an average loading of 3 mg cm^{-2}. The coated electrode was left at 600 °C for 2 h to fully calcine. To better understand the synergistic effect of Cu and Sb, samples were also synthesized either with copper oxide only (without antimony) or with antimony oxide only (without copper).

Physical characterizations

The chemical composition and elemental distribution map were determined using energy dispersive X-ray spectroscopy (EDS). The surface of the electrocatalysts was observed and imaged using a Mira3 TESCAN field emission scanning electron microscope (FESEM). To measure the thickness of the coating, the cross-section

of the electrode was examined using FESEM imaging and an EDS-mapping was used to accurately distinguish the coating from the substrate. Then, the layer thickness was measured and analyzed using ImageJ software at several points on the cross-section (according to ASTM B487). In addition, powder X-ray diffraction (PXRD) was performed to determine the electrocatalyst constituent phases. For this purpose, the copper- and antimony-containing solutions were placed in a furnace and the furnace temperature was increased to 600℃ at a heating rate of 1℃/s. Finally, they were held at 600℃ for 2 h to form the target compound powder. The diffraction pattern of the synthesized powder was then obtained using filtered Cu-K_α X-rays ($\lambda = 0.15418$ nm) at the angles of 20 to 80 degree. The stoichiometry of the electrocatalysts was determined by dissolving the catalyst powders in hydrochloric acid and measuring the concentration of dissolved ions using inductively coupled plasma mass spectrometry (ICP-MS). Absorption data for determining NO_3^- and NH_3 concentrations were obtained using a UV-vis spectrophotometer (HACH DR6000).

Electrochemical measurements

Electrochemical tests were performed in a custom H-cell (Fig. S2) in 0.1 M sodium hydroxide (NaOH) medium with and without 100 mM sodium nitrate ($NaNO_3$) using a standard three-electrode arrangement using an Autolab® PGSTAT 30. In the standard three-electrode arrangement, a platinum electrode as the auxiliary electrode was separated by a Nafion 115 membrane from a saturated Ag|AgCl electrode as the reference electrode and the synthesized electrocatalyst as the working electrode. The geometric area of the working electrode was 1 cm^2. The potential used in this study were reported as potential versus the reversible hydrogen electrode (RHE) using the following equation:

Linear sweep voltammetry (LSV) was performed to determine the activity and cathodic Tafel constant (β_c) of the electrocatalysts. The LSV was performed from the open circuit potential (OCP) to the potential of −1 vs. RHE at a scan rate of 1 mV s^{-1}. Cyclic voltammetry in the non-Faradaic current domain (± 0.2 V vs. OCP) was used to determine the double layer capacitance (C_{dl}) and to estimate the electrochemical active surface area (ECSA). Chronoamperometry was performed to measure the NH_3 yield and Faradaic Efficiency (F.E.). Electrochemical impedance spectroscopy (EIS) was performed to measure the charge transfer resistance (R_{ct}) of the electrocatalysts at a constant potential of −0.4 V vs. RHE with a voltage amplitude of 10 mV and a frequency range of 100 kHz to 10 mHz using a ZIVE SP1 potentiostat.

Conclusion

Low-cost copper antimonate electrocatalysts were synthesized using a sol-gel method for the NRA process. The influence of different molar ratios of antimony to copper on their performance in the NRA process was investigated. The results are as follows:

- XRD results showed that even in non-stoichiometric ratios of Sb to Cu in precursor solution, the main and, of course, stable phase is $CuSb_2O_6$. The XRD after the catalytic conversion reaction of nitrate to ammonium also confirmed that phases other than $CuSb_2O_6$ decompose and disappear over time.
- LSV curves showed that $CuSb_2O_x$ exhibits the best catalytic activity and, according to Tafel diagrams, $CuSb_2O_x$ has the lowest cathodic Tafel constant. It means that the $CuSb_2O_6$ phase, with a 2:1 ratio of antimony to copper, will present the least barrier to the nitrate reduction reaction.
- According to SACV and EIS results, $CuSb_2O_x$ exhibits the highest active sites and lowest charge transfer resistance in the NRA process at only $R_{ct} = 3.75\ \Omega\ cm^2$.
- Analysis of the CA results showed that the synthesized $CuSb_2O_x$ provided a high NH_3 yield of 7320 μg h^{-1} cm^{-2} and a high F.E. of 89% (−0.7 V vs. RHE) in alkaline medium with pH = 13.
- The selectivity of $CuSb_2O_x$ was increased during the NRA process, reaching 98.8% after 15 h of electrochemical conversion of NO_3^- to NH_3.
- According to the CA, XRD, and FESEM results, $CuSb_2O_x$ is an electrocatalyst with excellent stability for the NRA process.

This study presents a high-performance and non-precious electrocatalyst for the electrochemical conversion of NO_3-N to NH_3-N. Future studies should focus on further improving the selectivity of electrocatalysts for electrochemical NH_3 production from low-concentration NO_3^- sources.

Data availability

Data will be made available on request. If you need to receive data from this study, please send your request via email to the Corresponding Author (Milad Rezaei). All relevant data will be made available to applicants upon reasonable request.

Received: 13 October 2025; Accepted: 11 December 2025
Published online: 14 December 2025

References

1. Yao, F. et al. Highly selective electrochemical nitrate reduction using copper phosphide self-supported copper foam electrode: Performance, mechanism, and application. *Water Res.* **193**, 116881 (2021).
2. Hollevoet, L., De Ras, M., Roeffaers, M., Hofkens, J. & Martens, J. A. Energy-efficient ammonia production from air and water using electrocatalysts with limited Faradaic efficiency. *ACS Energy Lett.* **5** (4), 1124–1127 (2020).
3. Suryanto, B. H. et al. Challenges and prospects in the catalysis of electroreduction of nitrogen to ammonia. *Nat. Catal.* **2** (4), 290–296 (2019).
4. Cui, X., Tang, C. & Zhang, Q. A review of electrocatalytic reduction of dinitrogen to ammonia under ambient conditions. *Adv. Energy Mater.* **8** (22), 1800369 (2018).

5. Kitano, M. et al. Electride support boosts nitrogen dissociation over ruthenium catalyst and shifts the bottleneck in ammonia synthesis. *Nat. Commun.* **6** (1), 6731 (2015).
6. Liu, Y. et al. Pothole-rich ultrathin WO3 nanosheets that trigger N ≡ N bond activation of nitrogen for direct nitrate photosynthesis. *Angew. Chem. Int. Ed.* **58** (3), 731–735 (2019).
7. Ertl, G. Reactions at surfaces: from atoms to complexity. *Angew. Chem. Int. Ed.* **47** (19), 3524–3535 (2008).
8. Shipman, M. A. & Symes, M. D. Recent progress towards the electrosynthesis of ammonia from sustainable resources. *Catal. Today*. **286**, 57–68 (2017).
9. Hansen, T. W. et al. Atomic-resolution in situ transmission electron microscopy of a promoter of a heterogeneous catalyst. *Science* **294** (5546), 1508–1510 (2001).
10. Luo, Y. et al. Efficient electrocatalytic N2 fixation with Mxene under ambient conditions. *Joule* **3** (1), 279–289 (2019).
11. Singh, A. R. et al. Electrochemical ammonia Synthesis — The selectivity challenge. *ACS Catal.* **7** (1), 706–709 (2017).
12. Wang, J. et al. Nanodenitrification with bimetallic nanoparticles confined in N-doped mesoporous carbon. *Environ. Science: Nano*. **7** (5), 1496–1506 (2020).
13. Wang, J., Ling, L., Deng, Z. & Zhang, W. X. Nitrogen-doped iron for selective catalytic reduction of nitrate to dinitrogen. *Sci. Bull.* **65** (11), 926–933 (2020).
14. Wei, J. et al. Copper-based electro-catalytic nitrate reduction to ammonia from water: Mechanism, preparation, and research directions. *Environ. Sci. Ecotechnology*. **20**, 100383 (2024).
15. Marnellos, G. & Stoukides, M. Ammonia synthesis at atmospheric pressure. *Science* **282** (5386), 98–100 (1998).
16. Chinthaginjala, J. K. & Lefferts, L. Support effect on selectivity of nitrite reduction in water. *Appl. Catal. B*. **101** (1–2), 144–149 (2010).
17. Li, H. et al. Cu x Ir1–x Nanoalloy catalysts achieve near 100% selectivity for aqueous nitrite reduction to NH3. *ACS Catal.* **10** (14), 7915–7921 (2020).
18. Casella, I. G. & Contursi, M. Highly dispersed rhodium particles on multi-walled carbon nanotubes for the electrochemical reduction of nitrate and nitrite ions in acid medium. *Electrochim. Acta*. **138**, 447–453 (2014).
19. Zhang, X. et al. Recent advances in non-noble metal electrocatalysts for nitrate reduction. *Chem. Eng. J.* **403**, 126269 (2021).
20. Li, J. et al. Efficient ammonia electrosynthesis from nitrate on strained ruthenium nanoclusters. *J. Am. Chem. Soc.* **142** (15), 7036–7046 (2020).
21. Yang, J., Sebastian, P., Duca, M., Hoogenboom, T. & Koper, M. T. pH dependence of the electroreduction of nitrate on Rh and Pt polycrystalline electrodes. *Chem. Commun.* **50** (17), 2148–2151 (2014).
22. Jia, R. et al. Boosting selective nitrate electroreduction to ammonium by constructing oxygen vacancies in TiO2. *ACS Catal.* **10** (6), 3533–3540 (2020).
23. Wei, P. et al. Iron-doped Cobalt oxide nanoarray for efficient electrocatalytic nitrate-to-ammonia conversion. *J. Colloid Interface Sci.* **615**, 636–642 (2022).
24. Zeng, R. et al. Nonprecious transition metal nitrides as efficient oxygen reduction electrocatalysts for alkaline fuel cells. *Sci. Adv.* **8** (5), eabj1584 (2022).
25. Qi, D. et al. High-efficiency electrocatalytic NO reduction to NH 3 by nanoporous VN. *Nano Res. Energy*. **1** (2), e9120022 (2022).
26. Liang, J. et al. FeP Nanorod array: A high-efficiency catalyst for electroreduction of NO to NH3 under ambient conditions. *Nano Res.* **15** (5), 4008–4013 (2022).
27. Li, Z. et al. High-efficiency ammonia electrosynthesis via selective reduction of nitrate on ZnCo2O4 nanosheet array. *Mater. Today Phys.* **23**, 100619 (2022).
28. Zhao, X. et al. Comprehensive Understanding of the thriving electrocatalytic nitrate/nitrite reduction to ammonia under ambient conditions. *J. Energy Chem.* **92**, 459-483 (2024).
29. Li, J. et al. Boosting electrochemical nitrate-to-ammonia conversion by self-supported MnCo2O4 nanowire array. *J. Colloid Interface Sci.* **629**, 805–812 (2023).
30. Li, J. et al. Microenvironmental corrosion and hydrolysis induced two-dimensional heterojunction of copper oxide@ ferriferous oxide for efficient electrochemical nitrate reduction to ammonia. *Chem. Eng. J.* **471**, 144488 (2023).
31. Tang, Y., Liu, S., Guo, C., Liu, Y. & Tang, Z. Constructing a CoO–CuO x heterostructure for efficient electrochemical reduction of nitrate to ammonia. *Sustainable Energy Fuels*. **7** (20), 5039–5045 (2023).
32. Huang, P. et al. 3D Flower-Like zinc Cobaltite for electrocatalytic reduction of nitrate to ammonia under ambient conditions. *ChemSusChem* **15** (4), e202102049 (2022).
33. Hai, Y. et al. Ammonia Synthesis via Electrocatalytic Nitrate Reduction Using NiCoO2 Nanoarrays on a Copper Foam. *ACS Appl. Mater, Interfaces* **16** (9) 11431-11439 (2024).
34. Fontana, M. G. & Greene, N. D. *Corrosion engineering* (McGraw-hill, 2018).
35. Nikulin, A. Y. et al. Preparation and characterization of metastable trigonal layered MSb2O6 phases (M = Co, Ni, Cu, Zn, and Mg) and considerations on FeSb2O6. *Dalton Trans.* **46** (18), 6059–6068 (2017).
36. Maimone, D. T., Christian, A. B., Neumeier, J. J. & Granado, E. Lattice dynamics of A Sb2O6 (A = Cu, Co) with trirutile structure. *Phys. Rev. B*. **97** (10), 104304 (2018).
37. Prokofiev, A. V., Ritter, F., Assmus, W., Gibson, B. J. & Kremer, R. K. Crystal growth and characterization of the magnetic properties of CuSb2O6. *J. Cryst. Growth.* **247** (3–4), 457–466 (2003).
38. Maimone, D. T., Christian, A. B., Neumeier, J. J. & Granado, E. Coupling of phonons with orbital dynamics and magnetism in CuSb2O6. *Phys. Rev. B*. **97** (17), 174415 (2018).
39. Cerrón-Calle, G. A., Fajardo, A. S., Sánchez-Sánchez, C. M. & Garcia-Segura, S. Highly reactive Cu-Pt bimetallic 3D-electrocatalyst for selective nitrate reduction to ammonia. *Appl. Catal. B*. **302**, 120844 (2022).
40. Moreno-Hernandez, I. A., Brunschwig, B. S. & Lewis, N. S. Crystalline nickel, cobalt, and manganese antimonates as electrocatalysts for the Chlorine evolution reaction. *Energy Environ. Sci.* **12** (4), 1241–1248 (2019).
41. Garcia-Segura, S., Lanzarini-Lopes, M., Hristovski, K. & Westerhoff, P. Electrocatalytic reduction of nitrate: fundamentals to full-scale water treatment applications. *Appl. Catal. B*. **236**, 546–568 (2018).
42. Liu, D. et al. Recent advances in electrocatalysts for efficient nitrate reduction to ammonia. *Adv. Funct. Mater.* **33** (43), 2303480 (2023).
43. Zhang, S., Li, M., Li, J., Song, Q. & Liu, X. High-ammonia selective metal–organic framework–derived Co-doped Fe/Fe2O3 catalysts for electrochemical nitrate reduction. *Proc. Natl. Acad. Sci.* **119** (6), e2115504119 (2022).
44. Jung, W. et al. Synergistic bimetallic CuPd oxide alloy electrocatalyst for ammonia production from the electrochemical nitrate reaction. *J. Mater. Chem. A*. **10** (44), 23760–23769 (2022).
45. Yin, Q., Hu, S., Liu, J. & Zhou, H. Electrochemical ammonia synthesis via nitrate reduction on perovskite LaxFeO3 – δ with enhanced efficiency by oxygen vacancy engineering. *Sustainable Energy Fuels*. **6** (20), 4716–4725 (2022).
46. Chen, G. F. et al. Electrochemical reduction of nitrate to ammonia via direct eight-electron transfer using a copper–molecular solid catalyst. *Nat. Energy*. **5** (8), 605–613 (2020).
47. Zhang, X. et al. Cu clusters/TiO_{2-x} with abundant oxygen vacancies for enhanced electrocatalytic nitrate reduction to ammonia. *J. Mater. Chem. A*. **10** (12), 6448–6453 (2022).
48. Liang, J. et al. Amorphous Boron carbide on titanium dioxide nanobelt arrays for high-efficiency electrocatalytic NO reduction to NH_3. *Angew. Chem. Int. Ed.* **61** (18), e202202087 (2022).

49. Liu, M. et al. Electroreduction of nitrate to ammonia on palladium–cobalt–oxygen nanowire arrays. *ACS Appl. Mater. Interfaces.* **14** (11), 13169–13176 (2022).
50. Liu, X. et al. Heterostructured Bi2S3/MoS2 nanoarrays for efficient electrocatalytic nitrate reduction to ammonia under ambient conditions. *ACS Appl. Mater. Interfaces.* **14** (34), 38835–38843 (2022).
51. Babaei, A. & Rezaei, M. Development of a highly stable and active non-precious anode electrocatalyst for oxygen evolution reaction in acidic medium based on nickel and cobalt-containing antimony oxide. *J. Electroanal. Chem.* **935**, 117319 (2023).
52. de Oliveira-Sousa, A., Da Silva, M. A., Machado, S. A., Avaca, L. A. & de Lima-Neto, P. Influence of the Preparation method on the morphological and electrochemical properties of Ti/IrO_2-coated electrodes. *Electrochim. Acta.* **45** (27), 4467–4473 (2000).

Acknowledgements
The authors of this article are grateful to the Iran National Science Foundation (INSF) on the grant number 4032066.

Author contributions
AliReza Babaei: ** Methodology, Investigation, Data curation, Visualization, Writing – original draft. **Milad Rezaei: ** Supervision, Project Administration, Validation, Writing – review & editing. **Pirooz Marashi: ** Supervision, Validation, Writing – review & editing. **William Mark Rainforth : Formal Analysis, Writing – review & editing.

Declarations

Competing interests
The authors declare no competing interests.

Additional information
Supplementary Information The online version contains supplementary material available at https://doi.org/10.1038/s41598-025-32713-4.

Correspondence and requests for materials should be addressed to M.R.

Reprints and permissions information is available at www.nature.com/reprints.

Publisher's note Springer Nature remains neutral with regard to jurisdictional claims in published maps and institutional affiliations.